Linearity Measurement and Pulse Amplitude Modulation in a Silicon Single-Drive Push–Pull Mach–Zehnder Modulator

Yanyang Zhou, Linjie Zhou, *Member, IEEE*, Feiran Su, Xinwan Li, *Senior Member, IEEE*, and Jianping Chen

***Abstract*—We characterize the modulation linearity of a silicon Mach–Zehnder modulator with a single-drive push–pull configuration. The 3-dB electro-optic bandwidths of the modulator are 15 and 32 GHz at 0 and 6 V reverse biases, respectively. The best spurious-free dynamic ranges (SFDRs) for the second-order harmonic distortion and the third-order intermodulation distortion are measured to be 97.7 dB·Hz$^{2/3}$ and 85.9 dB·Hz$^{1/2}$. The experimental measurement demonstrates that such a drive scheme can effectively reduce the modulation nonlinearity, especially the second harmonic distortion. Multi-level pulse amplitude modulation (PAM) is achieved using this high-linearity modulator with PAM-2,3,4,5 at a symbol rate of 40 Gbaud/s and PAM-8 at a symbol rate of 25 Gbaud/s.**

***Index Terms*—Electrooptic modulator, microwave photonics, silicon photonics.**

I. Introduction

FOR optical modulators used in microwave photonics (MWP) systems and telecommunications such as photonic microwave filters [1], photonic phased array antennae [2], analog-to-digital converters [3], [4], and advanced modulation formats [5], [6], one of the important metrics to measure their performances is the linearity, which is characterized by the spurious-free dynamic range (SFDR) [7]. Though Mach–Zehnder modulators (MZMs) based on Lithium Niobate ($LiNbO_3$) or III–V semiconductors have a higher SFDR (up to 121 dB·Hz$^{2/3}$ for the former [8] and 128 dB·Hz$^{2/3}$ for the latter [9]), they have a large footprint and are also difficult to integrate with electronic circuits. Optical modulators made on the silicon platform surpass them as they are compatible with the complementary metal oxide semiconductor (CMOS) techniques for low-cost fabrication and monolithic integration with microelectronics on one single chip. In fact, silicon modulators have been developing rapidly in recent years [10]. For example, carrier-depletion-based MZMs have been demonstrated with an operation speed up to 40 Gb/s [11]–[18].

Manuscript received October 06, 2015; revised April 23, 2016 and March 01, 2016; accepted May 05, 2016. Date of publication May 10, 2016; date of current version June 22, 2016. This work was supported in parts by the 973 program (ID2011CB301700), the 863 program (2013AA014402), the National Natural Science Foundation of China (NSFC) (61422508, 61535006), and SRFDP of MOE (Grant No. 20130073130005).

The authors are with the State Key Laboratory of Advanced Optical Communication Systems and Networks, Department of Electronic Engineering, Shanghai Jiao Tong University, Shanghai 200240, China (e-mail: zhouyanyang88@sjtu.edu.cn; ljzhou@sjtu.edu.cn; ssaviour@sjtu.edu.cn; lixinwan@sjtu.edu.cn; jpcheng62@sjtu.edu.cn).

Color versions of one or more of the figures in this paper are available online at http://ieeexplore.ieee.org.

Digital Object Identifier 10.1109/JLT.2016.2567067

In order to improve the linearity of silicon optical modulators, many methods have been proposed and demonstrated. Khilo *et al*. have demonstrated that, under the differential detection and push–pull drive scheme with a proper operation point for a certain phase shifter length, the SFDR for the second-order harmonic distortion ($SFDR_{SHD}$) and the SFDR for the third-order intermodulation distortion ($SFDR_{IMD}$) can be canceled and the linearity of silicon MZM can be theoretically larger than that of conventional $LiNbO_3$ MZM [19]. Recent research shows that by using differential drive, the linearity of silicon MZM can be improved to 82 dB·Hz$^{1/2}$ for $SFDR_{SHD}$ and 97 dB·Hz$^{2/3}$ for $SFDR_{IMD}$ [20]. Microring modulators have been demonstrated to exhibit a $SFDR_{IMD}$ of 84 dB·Hz$^{2/3}$, but it is not suitable for wideband microwave systems due to the poor $SFDR_{SHD}$ [21], [22]. $SFDR_{IMD}$ of 106 dB·Hz$^{2/3}$ has been achieved in ring-assisted MZMs [23], [24], because the phase response of the ring resonator cancels the nonlinearity in the MZI sinusoidal transfer function.

In this paper, we present a silicon MZM with a single-drive push–pull traveling-wave electrode (TWE) configuration with improved linearity. The TWE is optimized to provide impedance match and flat electro-optic response. Compared with conventional differential drive, the single-drive scheme can more effectively reduce the second-order harmonic distortion due to the two auto-aligned push–pull signals from one RF feed. The $SFDR_{SHD}$ is measured to be 85.9 dB·Hz$^{1/2}$ with 3.9 dB improvement over the previous best result [20] and the $SFDR_{IMD}$ is measured to be 97.7 dB·Hz$^{2/3}$. Due to its high linearity, the modulator can generate 2, 3, 4, 5-level pulse amplitude modulation (PAM) signals at the symbol rate of 40 Gbaud/s and a 8-level PAM signal at the symbol rate of 25 Gbaud/s.

II. Device Design and Fabrication

Fig.1(a) shows the schematic structure of our silicon MZM. Compared to the differential drive configuration, the single-drive features low chirp, low capacitance (two junction capacitors connected in series), and simplified RF connection interface [25], [26]. The length difference of two arms in the asymmetric MZI is 90 μm. The 3.3-mm-long TWE uses a symmetric coplanar strip (CPS) structure in a ground-signal (GS) configuration with the two metal strips connected to the p^+-doping regions outside the MZI arms where the RF signal is applied. A dc voltage (V_d) is applied to the middle n^+-doping region to set the two p-n junctions at the reverse-bias mode. The silicon waveguide is 500 nm wide and 220 nm high with an etched depth of

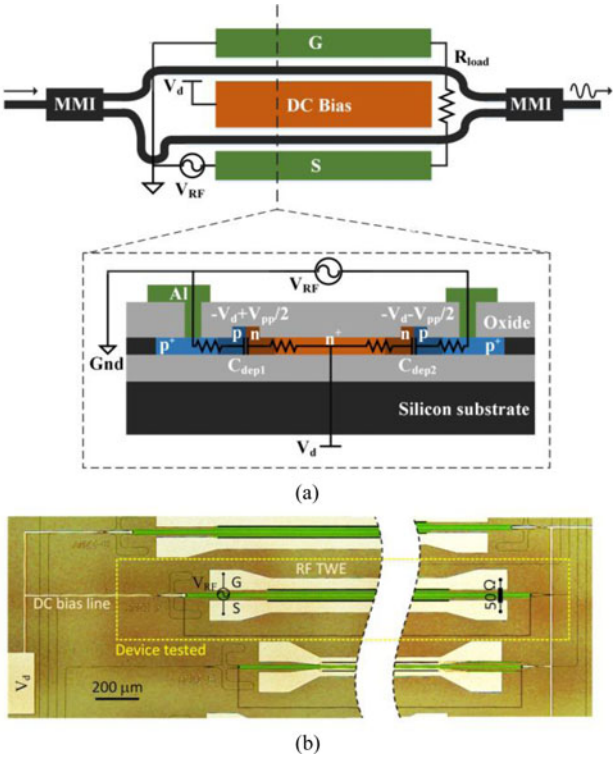

Fig. 1. (a) Schematic structure of the MZM. Inset shows the cross-section of the TWE and the circuit model. (b) Optical microscope image of the MZM.

160 nm. The p-n junction is positioned in the middle of the silicon waveguide with doping concentrations of $\sim 4 \times 10^{17}\ \mathrm{cm}^{-3}$ and $\sim 1 \times 10^{18}\ \mathrm{cm}^{-3}$ for the p- and n-doping regions, respectively. Inverse tapers are used at the waveguide ends for optical input- and output-coupling.

Fig. 1(b) shows the optical microscope image of the fabricated device. The p-n junction is segmented with a 1-μm-long striation un-doped in every 10 μm length to ensure that current flows only in the metal strips to reduce the RF loss. The TWE is made of aluminum metal strips with a width of 60 μm and a thickness of 1.5 μm. The gap separation between the signal and ground metal lines is 50 μm. The dc bias line is connected to the middle n^+-doping region. In order to reduce the electromagnetic interference between the RF and dc signals, the dc line is designed as 10 μm wide and 2 mm long to act as an inductor to isolate them. As shown in Fig. 1(a), the two PN junctions are connected in series with the dc voltage applied to the common cathode of the PN junctions to set the reverse bias at V_d. An RF drive signal V_{RF} is applied onto one end of the TWE (the G and S metal lines). The other end is terminated with an external 50 Ω resistor. It should be noted that a common ground is used for both the RF signal and dc bias and hence the dc voltage drop is on both PN junctions. Assuming the PN junction capacitances are equal ($C_{\mathrm{dep1}} = C_{\mathrm{dep2}}$), then the RF voltage drop on each PN junction is $V_{\mathrm{RF}}/2$. Because the two PN junctions are connected back-to-back, the RF voltage drop has an opposite sign. Therefore, the entire voltage drop is $-V_d + V_{\mathrm{RF}}/2$ on the left junction and $-V_d - V_{\mathrm{RF}}/2$ on the right junction, resulting in push–pull modulation at the reverse bias voltage V_d.

III. Linearity Analysis

This section presents a mathematical analysis of the linearity of the MZM. We assume that the MZM is composed of two ideal multimode interference (MMI) 3-dB couplers. The output electric field can be expressed as

$$E_{\mathrm{out}} = \frac{E_{\mathrm{in}}}{2}\left[e^{-a_A}\, e^{i(\phi_A+\Delta\phi)} + e^{-a_B}\, e^{i\phi_B}\right] \tag{1}$$

where $a_{A,B}$ and $\phi_{A,B}$ are the optical loss coefficient and the modulation phase shift of the MZI active arms (denoted by the subscript A and B) and $\Delta\phi$ is the phase difference between the two arms. At the quadrature and the peak transmission operation points, the $\Delta\phi$ is equal to $\pi/2$ and 0, respectively. The output powers for the two cases are given by

$$P_{\mathrm{out}}|_{\mathrm{Quad}} = P_{\mathrm{in}}\left[\frac{1}{4}(e^{-2a_A} + e^{-2a_B}) - \frac{1}{2}e^{-(a_A+a_B)}\sin(\phi_A-\phi_B)\right] \tag{2}$$

$$P_{\mathrm{out}}|_{\mathrm{Peak}} = P_{\mathrm{in}}\left[\frac{1}{4}(e^{-2a_A} + e^{-2a_B}) + \frac{1}{2}e^{-(a_A+a_B)}\cos(\phi_A-\phi_B)\right]. \tag{3}$$

$a_{A,B}$ and $\phi_{A,B}$ can be expanded to the third order polynomial of the RF drive voltage V as:

$$a_{A,B}(V) = a_0 + a_1 V + a_2 V^2 + a_3 V^3 \tag{4}$$

$$\phi_{A,B}(V) = \varphi_1 V + \varphi_2 V^2 + \varphi_3 V^3. \tag{5}$$

We assume the top and bottom arms have identical responses to drive voltage in the ideal case. During the push–pull modulation, the top and bottom arms are subject to opposite drive voltages of V and $-V$, respectively, and thus we have:

$$a_A + a_B = 2a_0 + 2a_2 V^2 \tag{6}$$

$$\phi_A - \phi_B = 2\varphi_1 V + 2\varphi_3 V^3. \tag{7}$$

Therefore, (2) and (3) can be rewritten as:

$$P_{\mathrm{out}}|_{\mathrm{Quad}} = P_{\mathrm{in}}\left[\frac{1}{4}\left(e^{-2(a_0+a_1V+a_2V^2+a_3V^3)} + e^{-2(a_0-a_1V+a_2V^2-a_3V^3)}\right) - \frac{1}{2}e^{-2(a_0+a_2V^2)}\sin(2\varphi_1V+2\varphi_3V^3)\right] \tag{8}$$

$$P_{\mathrm{out}}|_{\mathrm{Peak}} = P_{\mathrm{in}}\left[\frac{1}{4}\left(e^{-2(a_0+a_1V+a_2V^2+a_3V^3)} + e^{-2(a_0-a_1V+a_2V^2-a_3V^3)}\right) + \frac{1}{2}e^{-2(a_0+a_2V^2)}\cos(2\varphi_1V+2\varphi_3V^3)\right] \tag{9}$$

From the above equations, we see that three factors contribute to the nonlinearity: (i) optical loss modulation in the active arms, (ii) cubic nonlinearity of the phase modulation, and (iii) MZI sinusoidal transfer function.

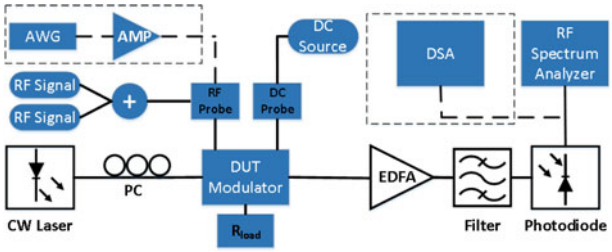

Fig. 2. Experimental setup to perform the MZM nonlinearity measurement and PAM-N (N = 2, 3, 4, 5, and 8) modulation.

The RF drive signal with two frequency tones can be written as $V = V_0 cos(\omega_1 t) + V_0 cos(\omega_2 t)$. With Taylor expansion and Jacobi–Anger expansion, the second term in the bracket of Eq. (8) can be rewritten as

$$\begin{aligned} & e^{-}2\left(a_0 + a_2 V^2\right) \sin\left(2\varphi_1 V + 2\varphi_3 V^3\right) \\ & \quad = A\left[\cos(2\omega_1 - \omega_2)t + \cos(2\omega_2 - \omega_1)t\right] \\ & \qquad + B\left[\cos(\omega_1 t) + \cos(\omega_2 t)\right] \qquad (10) \\ & A = e^{-2a_0}\left[(7a_2 V_0^2 - 2)J_1(z)J_2(z) - 3a_2 V_0^2 J_0(z)J_1(z)\right. \\ & \qquad \left. + 2a_2 V_0^2 J_0(z)J_3(z) - 3a_2 V_0^2 J_2(z)J_3(z)\right] \qquad (11) \\ & B = e^{-2a_0}\left[(2 - 9a_2 V_0^2)J_0(z)J_1(z) + 6a_2 V_0^2 J_1(z)J_2(z)\right. \\ & \qquad \left. + a_2 V_0^2 J_0(z)J_3(z)\right] \qquad (12) \end{aligned}$$

and the second term in the bracket of Eq. (9) can be rewritten as

$$\begin{aligned} & \mathrm{e}^{-2\left(a_0 + a_2 V^2\right)} \cos\left(2\varphi_1 V + 2\varphi_3 V^3\right) \\ & \quad = C\left[\cos\left(2\omega_1 t\right) + \cos\left(2\omega_2 t\right)\right] \qquad (13) \\ & C = e^{-2a_0}\left[4a_2 V_0^2 J_1^2(z) - a_2 V_0^2 J_0^2(z) - 2a_2 V_0^2 J_2^2(z)\right. \\ & \qquad \left. -2\left(1 - 2a_2 V_0^2\right) J_0(z) J_2(z)\right] \qquad (14) \end{aligned}$$

where $J_n(z)(n = 1, 2, 3)$ is the Bessel function, and $z = 2\varphi_1 V_0 + 3\varphi_3 V_0^3/2$. As pointed out in Ref. [19], at the quadrature operation point, SHD is completely cancelled by using the push–pull drive configuration. The conventional push–pull scheme needs two input RF signals with the exactly inversed phases. However, a slight length mismatch between the two input cables can cause the two signals desynchronized, leading to imperfect nonlinearity cancellation. The single-drive scheme cannot improve the linearity of the modulator compared to the push–pull scheme in theory, but it can generate the push–pull signals free of synchronization (the two drive signals are automatically matched), which can guarantee low SHD. The free-carrier absorption modulation in active arms also induces SHD and IMD. One approach to reduce these nonlinearities is to shift the operation point slightly away from quadrature point, so the quadratic term in the sine transfer function can compensate the nonlinearity of loss [19]. If the modulator is biased at the peak transmission point, modulation generates the SHD with the fundamental and IMD tones eliminated as suggested by (13). Therefore, in order to get a large SFDR, the MZ modulator needs to operate near the quadrature bias point.

IV. Experiments and Results

Fig. 2 shows the experimental setup to measure the SFDR and perform the PAM-N (N = 2, 3, 4, 5 and 8) modulation. Light from a tunable continuous wave (CW) laser first went through a polarization controller to set the transverse electric (TE) polarization and coupled to the MZM through an on-chip inverse taper. The modulated light was amplified by an erbium-doped fiber amplifier (EDFA) to compensate for MZM insertion loss and followed by a 3-nm bandwidth optical filter to suppress the amplified spontaneous emission (ASE) noise. The light was finally received by a 100 GHz bandwidth photodetector (u^2t XPDV4120R). The responsivity of the photodetector is 0.5 A/W. For the SFDR measurement, the MZM was driven by a microwave signal consisting of two tones at frequencies 1005 and 1015 MHz generated by a microwave generator (R&S SMB100A). The microwave signal was applied to the TWE of the MZM via a 40 GHz bandwidth microwave GS probe. The other end of TWE was terminated with a 50 Ω resistor. The SFDR was obtained by measuring the fundamental, SHD and IMD components on an RF spectrum analyzer (R&S FSUP50). For the PAM modulation, a 20-GHz arbitrary waveform generator (AWG) from Keysight (M8195A) was used as the RF drive signal to modulate the MZM and the modulated signal was measured by a 33-GHz real-time digital signal analyzer (DSA) from Keysight (DSAX93204A).

We first measured the MZM optical transmission spectra with the reverse bias applied either to the top or the bottom arms. Fig. 3(a) shows the typical spectra at 0 V and 6 V reverse biases. The spectra are all normalized to a passive straight waveguide. The on-chip insertion loss of the modulator is around 9 dB. The free spectral range (FSR) is 6.3 nm.

From the spectral shift, we can get the relative phase shift (ϕ) versus reverse bias as shown in Fig. 3(b). The small-signal π phase change voltage V_π is obtained according to the following equation:

$$V_\pi \left.\frac{d\phi}{dV}\right|_{V=V_d} = \pi. \qquad (15)$$

Therefore, the modulation efficiencies of the top and bottom arms at $V_d = 0$ V are $V_\pi L = 0.98$ V·cm and 1.23 V·cm, respectively.

One sees from Fig. 3(a) that the extinction ratio (ER) of the interference fringe increases when the bias is applied to the top arm while it decreases when the bias at the bottom arm. Thus, it is inferred that the top arm has a higher loss than the bottom one, i.e., $a_A > a_B$. The loss imbalance of the two arms is probably caused by the fabrication imperfection. The ER (in dB unit) of the interference fringe is expressed as

$$ER = 20\log_{10}\left(\frac{\mathrm{e}^{-a_B} + \mathrm{e}^{-a_A}}{\mathrm{e}^{-a_B} - \mathrm{e}^{-a_A}}\right). \qquad (16)$$

Therefore, we have

$$\frac{\mathrm{e}^{-a_B} + \mathrm{e}^{-a_A}}{\mathrm{e}^{-a_B} - \mathrm{e}^{-a_A}} = 10^{\frac{\mathrm{ER}}{20}} \equiv k \qquad (17)$$

$$a_A - a_B = \ln\frac{k+1}{k-1}. \qquad (18)$$

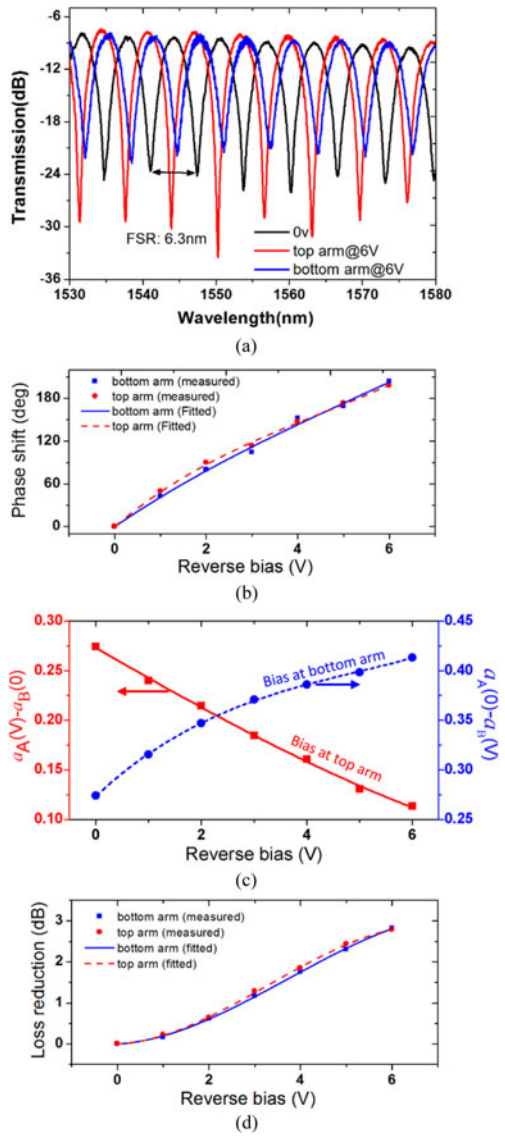

Fig. 3. (a) Optical transmission spectra at 0 V and 6 V reverse biases. (b) Phase shift of top and bottom arms versus reverse bias. (c) Relative loss coefficient change with reverse bias. The dots are measured data and lines are polynomial fitting curves. (d) Loss reduction of top and bottom arms versus reverse bias.

From the measured ER change with bias on the top or bottom arm, we can get $a_A(V) - a_B(0)$ or $a_A(0) - a_B(V)$ as a function of reverse bias voltage *V*, respectively, as shown in Fig. 3(c).

The optical phase shift and loss versus voltage for each arm are fit with a third-order polynomial. The fitting parameters for each arm of the MZM are listed in Table I.

We can convert the loss coefficient change into waveguide loss change by using the following formula:

$$\Delta Loss_{A,B}\,(dB) = 20\left[a_{A,B}(V) - a_{B,A}(0)\right]\log_{10} e. \quad (19)$$

Fig. 3(d) shows the loss reduction as a function of reverse bias for the top and bottom arms. The loss reduction rate is similar for the two arms.

The TWE was optimized to achieve a large electro–electro (EE) bandwidth [26]. The measured S-parameters (S_{21} and S_{11}) under various bias voltages are shown in Figs. 4(a) and 4(b). The

TABLE I
FITTING PARAMETERS FOR EACH ARM OF THE MZM

Coefficients	Top Arm	Bottom Arm
φ_1 (deg/V)	54.7313	43.8448
φ_2 (deg/V^2)	−6.5610	−2.6713
φ_3 (deg/V^3)	0.4945	0.1664
a_1 (/V)	−0.04891	−0.03194
a_2 (/V^2)	0.0071	6.21E-4
a_3 (/V^3)	−4.67E-4	3.38E-5

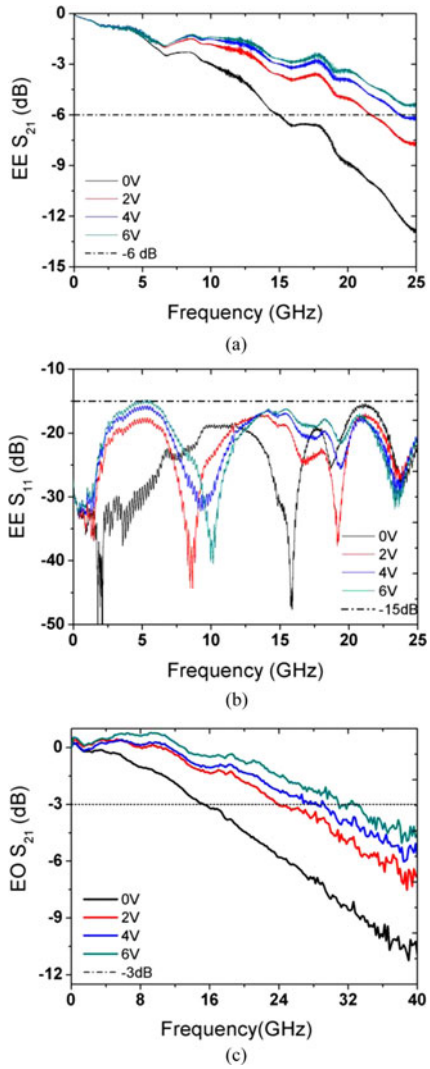

Fig. 4. (a) EE transmission response S_{21} of the TWE. (b) EE reflection response S_{11} of the TWE. (c) EO transmission response S_{21} of the MZM.

microwave probe and coaxial cables were calibrated before measurement using the standard short-open-load-through (SOLT) method. The 6-dB EE bandwidth increases from 14.2 GHz at $V_d = 0V$ to 23 GHz at $V_d = 4V$, as observed from the S_{21} curves of the TWE. The microwave reflection at the entrance of the TWE due to impendence mismatch is represented by the EE S_{11} curves. The measured S_{11} is below −15 dB, suggesting very low reflection in the frequency range from 10 MHz to 26.5 GHz and hence good impedance match with 50 Ω. We also measured

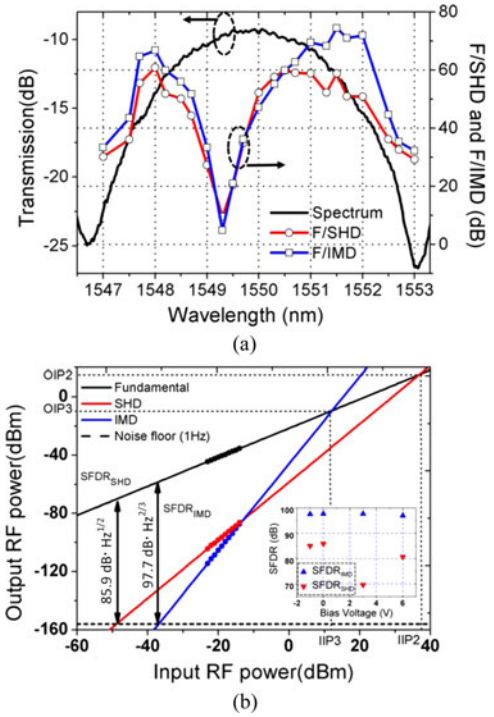

Fig. 5. (a) Measured transmission spectra and the ratios of F/SHD and F/IMD as function of wavelength. (b) SFDR of the MZM at the quadrature operation point (1551.5 nm). The dots represent the measured data. The straight lines are the linear fitting lines. Inset shows the $\mathrm{SFDR_{IMD}}$ and $\mathrm{SFDR_{SHD}}$ measured at various bias voltages.

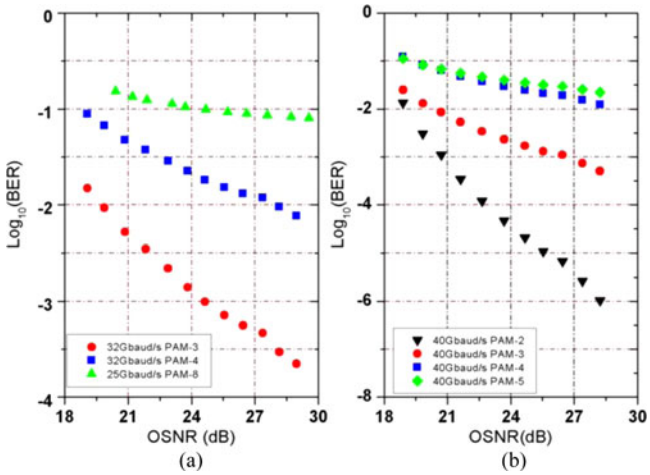

Fig. 6. Measured BER as a function of OSNR. (a) The BER of PAM-3,4 at 32 Gbaud/s and the BER of PAM-8 at 25Gbaud/s. (b) The BER of PAM-3,4,5 at 40 Gbaud/s.

the small signal EO response of the modulator by using a lightwave component analyzer (LCA) which covers the frequency range from 100 MHz to 40 GHz. As shown in Fig. 4(c), the measured EO 3-dB bandwidth is 15 GHz at $V_d = 0$ V and increases to 32 GHz at $V_d = 6$ V. The EO response is relatively flat from 3 GHz and 13 GHz when $V_d \geq 2$ V, which is useful for the wideband microwave photonics applications such as analog-to-digital converters.

In order to find the optimal operation point to achieve the highest SFDR, we measured the output power ratio between the fundamental tones and the distortions (F/SHD and F/IMD) versus wavelength as shown in Fig. 5(a). The power of the fundamental tone at each wavelength was set to –50 dBm. Both traces F/SHD and F/IMD have two peaks at the positive and negative slopes of the optical transmission spectrum close to the quadrature operation points. Because of the nonlinearity of free carrier absorption loss and the fact that loss and phase responses of the two arms are slightly different due to fabrication imperfections, the SHD cannot be fully cancelled when the modulator is biased at quadrature. The input laser wavelength was set at the quadrature point (1551.5 nm) for the following linearity measurement. The optical power received by the photodetector was 12 dBm and the photodetector current was 8.58 mA. The bias voltage was set to $V_d = 0$ V. We measured the output signals including fundamental, SHD, and IMD with 10 Hz resolution bandwidth and the noise floor observed from the RF spectrum analyzer was –146 dBm, mainly contributed by shot noise, thermal noise and source laser intensity noise. SFDR was obtained by measuring the fundamental, SHD, IMD tones when the power of two input tones varies, as shown in Fig. 5(b). Ten data points were used to fit the curves of the fundamental, SHD, and IMD. The fundamental tone has a linear response to the input power with a slope of 0.996. The SHD has a quadratic response to the input power with a slope of 1.997. The IMD power has a cubic response to the input power with a slope of 2.987. The noise floor is at –156 dBm with 1 Hz resolution bandwidth. The $\mathrm{SFDR_{SHD}}$ and $\mathrm{SFDR_{IMD}}$ for this single-drive push–pull MZM at 0 V bias are hence 85.9 ± 0.45 dB·Hz$^{1/2}$ and 97.7 ± 0.55 dB·Hz$^{2/3}$, respectively. Compared with the modulator with a differential drive configuration [20], a 3.9 dB improvement for $\mathrm{SFDR_{SHD}}$ has been achieved. The input intercept points (IIP2: 36.9 dBm, IIP3: 12.2 dBm) and the output intercept points (OIP2: 15.22 dBm, OIP3: –9.4 dBm) represent the input and output powers respectively when the fundamental tone curve intersects the SHD and IMD curves. We also measured the bias dependence of the SFDR. The inset of Fig. 5(b) shows that the $\mathrm{SFDR_{SHD}}$ is sensitive to the bias while the $\mathrm{SFDR_{IMD}}$ is almost independent of the bias [7].

The high linearity property of the modulator can be exploited to generate PAM modulation signals. The input laser wavelength was set at the quadratic point to ensure the modulator was operated in the linear response regime. The RF drive signal from the AWG was amplified to a voltage swing of 7 V_{pp}. The bias voltage was set at 6 V. The bit error rate (BER) of the PAM signals as a function of optical signal-to-noise ratio (OSNR) was used to evaluate the modulation performance as shown in Fig. 6. Compared to a commercial $LiNbO_3$ modulator [27], this modulator shows about 3 dB OSNR penalty to achieve 1e-6 BER for 40 Gbaud/s PAM-2 modulation. Fig. 7(a) – 7(f) show the eye diagrams for PAM-N (N = 2, 3, 4, 5) modulations at symbol rates up to 40 Gbaud/s. The PAM-3 and PAM-4 modulations exhibit clear eye diagrams at 32 Gbaud/s yet slightly deteriorated at 40 Gbaud/s, partially limited by the low bandwidth of the DSA (33 GHz bandwidth). PAM-8 modulation was achieved at 25 Gbaud/s as shown in Fig. 6(f). A clearer eye-diagram could

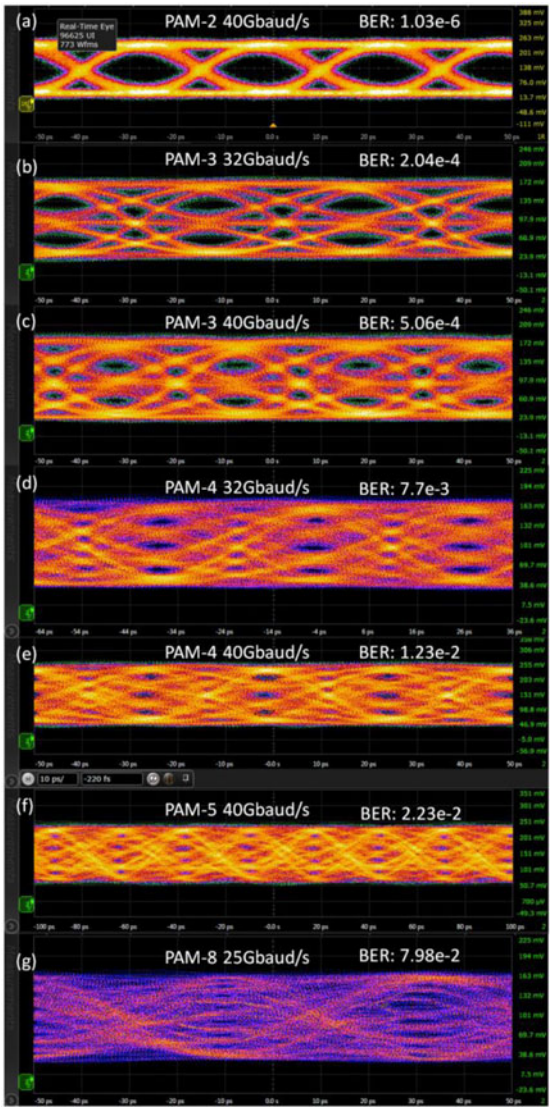

Fig. 7. Measured eye-diagrams of the PAM-N (N = 2,3,4,5, and 8) modulated optical signals.

be obtained by using a higher bandwidth DSA assisted with post signal processing, such as pre-emphasis and equalization.

V. Conclusion

We have presented experimental measurement on the linearity of a carrier-depletion-based silicon MZM with a single-drive push–pull drive configuration. The single-drive scheme can effectively reduce the second harmonic distortion due to the two strictly aligned push–pull signals from the one input RF feed. The MZM possesses a 3-dB EO bandwidth of 15 and 32 GHz at 0 and 6 V reverse biases, respectively. The $SFDR_{SHD}$ and $SFDR_{IMD}$ were measured to be 85.9 $dB{\cdot}Hz^{1/2}$ and 97.7 $dB{\cdot}Hz^{2/3}$ at the quadrature operation point, respectively. PAM modulation was realized using the high-linearity modulator. Eye-diagrams were measured for the PAM-2, 3, 4, and 5 signals at a symbol rate of 40 Gbaud/s and the PAM-8 signal at a symbol of 25 Gbaud/s.

Acknowledgment

The authors would like to thank IME Singapore for device fabrication.

References

[1] M. Gutierrez, P. Sanchis, A. Brimont, D. J. Thomson, F. Y. Gardes, G. T. Reed *et al.*, "A photonic microwave filter based on an asymmetric silicon Mach-Zehnder modulator," *IEEE Photon. J.*, vol. 5, no. 4, pp. 550–1006, Aug. 2013.

[2] P. Wu, S. Tang, and D. E. Raible, "A prototype high-speed optically-steered X-band phased array antenna," *Opt. Exp.*, vol. 21, no. 26, pp. 32599–32604, Dec. 2013.

[3] G. C. Valley, "Photonic analog-to-digital converters," *Opt. Exp.*, vol. 15, no. 5, pp. 1955–1982, Mar. 2007.

[4] A. Khilo, S. J. Spector, M. E. Grein, A. H. Nejadmalayeri, C. W. Holzwarth, M. Y. Sander *et al.*, "Photonic ADC: Overcoming the bottleneck of electronic jitter," *Opt. Exp.*, vol. 20, no. 4, pp. 4454 –4469, Feb. 2012.

[5] R. Palmer, L. Alloatti, D. Korn, P. C. Schindler, R. Schmogrow, W. Heni *et al.*, "Silicon-organic hybrid MZI modulator generating OOK, BPSK and 8-ASK signals for up to 84 Gbit/s," *IEEE Photon. J.*, vol. 5, no. 2, pp. 6600907, Apr. 2013.

[6] M. Chagnon, M. Osman, M. Poulin, C. Latrasse, J. F. Gagne, Y.Painchaud *et al.*, "Experimental study of 112 Gb/s short reach transmission employing PAM formats and SiP intensity modulator at 1.3 μm," *Opt. Exp.*, vol. 22, no. 17, pp. 21018–21036, Aug. 2014.

[7] D. Marpaung, C. Roeloffzen, R. Heideman, A. Leinse, S. Sales, and J. Capmany, "Integrated microwave photonics," *Laser Photon. Rev.*, vol. 7, no. 4, pp. 506–538, 2013.

[8] A. Karim and J. Devenport, "Noise figure reduction in externally modulated analog fiber-optic links," *IEEE Photon. Technol. Lett.*, vol. 19, no. 5, pp. 312–314, Mar. 2007.

[9] B. Liu, J. Shim, Y.-J. Chiu, A. Keating, J. Piprek, and J. E. Bowers, "Analog characterization of low-voltage MQW traveling-wave electroabsorption modulators," *J. Lightw. Technol.*, vol. 21, no. 12, pp. 3011–3019, Dec. 2003.

[10] G. T. Reed, G. Mashanovich, F.Y. Gardes, and D. J. Thomson, "Silicon optical modulators," *Nature Photon*., vol. 4, no. 8, pp. 518–526, Jul. 2010.

[11] A. Liu, L. Liao, D. Rubin, H. Nguyen, B. Ciftcioglu, Y. Chetrit *et al.*, "High-speed optical modulation based on carrier depletion in a silicon waveguide," *Opt. Exp.*, vol. 15, no. 2, pp. 660–668, Jan. 2007.

[12] D. Thomson, F. Gardes, Y. Hu, G. Mashanovich, M. Fournier, P. Grosse *et al.*, "High contrast 40Gbit/s optical modulation in silicon," *Opt. Exp.*, vol. 19, no. 12, pp. 11507–11516, Jun. 2011.

[13] P. Dong, L. Chen, and Y. k. Chen, "High-speed low-voltage single-drive push-pull silicon Mach-Zehnder modulators," *Opt. Exp.*, vol. 20, no. 6, pp. 6163–6169, Mar. 2012.

[14] T. Baehr-Jones, R. Ding, Y. Liu, A. Ayazi, T. Pinguet, N. C. Harris *et al.*, "Ultralow drive voltage silicon traveling-wave modulator," *Opt. Exp.*, vol. 20, no. 11, pp. 12014–12020, May. 2012.

[15] A. Brimont, A. M. Gutierrez, M. Aamer, D. J. Thomson, F. Y. Gardes, J. Fedeli, G. T. Reed, J. Marti, and P. Sanchis, "Slow-light-enhanced silicon optical modulators under low-drive-voltage operation," *IEEE Photon. J.*, vol. 4, no. 5, pp. 1306–1315, Oct. 2012.

[16] J. Ding, R. Ji, L. Yang, and L. Yang "Electro-optical response analysis of a 40 Gb/s silicon Mach-Zehnder optical modulator," *J. Lightw. Technol.*, vol. 31, no. 14, pp. 2434–2440, Jul. 2013.

[17] M. Streshinsky, R. Ding, Y. Liu, A. Novack, Y. Yang, Y. Ma *et al.*, "Low power 50 Gb/s silicon traveling wave Mach-Zehnder modulator near 1300 nm," *Opt. Exp.*, vol. 21, no. 25, pp. 30350–30357, Dec. 2013.

[18] H. Xu, X. Li, X. Xiao, P. Zhou, Z. Li, J. Yu *et al.*, "High-speed silicon modulator with band equalization," *Opt. Lett.*, vol. 39, no. 16, pp. 4839–4842, Aug. 2014.

[19] A. Khilo, C. M. Sorace, and F. X. Kärtner, "Broadband linearized silicon modulator," *Opt. Exp.*, vol. 19, no. 5, pp. 4485–4500, Feb. 2011.

[20] M. Streshinsky, A. Ayazi, Z. Xuan, A. E.-J. Lim, G.-Q. Lo, T. Baehr-Jones *et al.*, "Highly linear silicon traveling wave Mach-Zehnder carrier depletion modulator based on differential drive," *Opt. Exp.*, vol. 21, no. 3, pp. 3818–3825, Feb. 2013.

[21] M. Song, L. Zhang, R. G. Beausoleil, and A. E. Willner, "Nonlinear distortion in a silicon microring-based electro-optic modulator for analog optical links," *IEEE J. Sel. Topics Quantum Electron.*, vol. 16, no. 1, pp. 185–191, Feb. 2010.

[22] A. Ayazi, T. Baehr-Jones, Y. Liu, A. E.-J. Lim, and M. Hochberg, "Linearity of silicon ring modulators for analog optical links," *Opt. Exp.*, vol. 20, no. 12, pp. 13115–13122, Jun. 2012.
[23] X. Xie, J. Khurgin, J. Kang, and F.-S. Chow, "Linearized Mach-Zehnder intensity modulator," *IEEE Photon. Technol. Lett.*, vol. 15, no .4, pp. 531–533, Apr. 2003.
[24] J. Cardenas, P. A. Morton, J. B. Khurgin, A. Griffith, C. B. Poitras, K. Preston *et al.*, "Linearized silicon modulator based on a ring assisted Mach Zehnder inteferometer," *Opt. Exp.*, vol. 21, no. 19, pp. 22549–22557, Sep. 2013.
[25] L. Chen, P. Dong, and Y.-K. Chen, "Chirp and dispersion tolerance of a single-drive push–pull silicon modulator at 28 Gb/s," *IEEE Photon. Technol. Lett.*, vol. 24, no. 11, pp. 936–938, Jun. 2012.
[26] J. Wang, L. Zhou, H. Zhu, R. Yang, Y. Zhou, L. Liu, T. Wang, and J. Chen, "Silicon high-speed BPSK modulator with a single-drive push-pull high speed travelling wave electrode," *Photon. Res.* vol. 3, no. 3, pp. 58–62, Jun. 2015.
[27] R. Ding, Y. Liu, Y. Ma, Y. Yang, Q. Li, A. E.-J. Lim, G.-Q. Lo, K. Bergman, T. Baehr-Jones, and M. Hochberg, "High-speed silicon modulator with slow-wave electrodes and fully independent differential drive," *J. Lightw. Technol.*, vol. 32, no. 12, pp. 2240–2247, Jun. 2014.

Yanyang Zhou received the B.S. degree in electrical engineering from Information Engineering University, Zhengzhou, China, in 2011. He is currently working toward the Ph.D. degree with the State Key Laboratory of Advanced Optical Communication Systems and Networks, Department of Electronic Engineering, Shanghai Jiao Tong University, Shanghai, China. His research interests include design of silicon modulators, optical communication systems.

Linjie Zhou (M'15) received the B.S. degree in microelectronics from Peking University, Beijing, China, in 2003, and the Ph.D. degree in electronic and computer engineering from the Hong Kong University of Science and Technology, Clear Water Bay, Hong Kong, in 2007. From 2007 to 2009, he was a Postdoctoral Researcher at the University of California, Davis. He is currently a Professor at the State Key Laboratory of Advanced Optical Communication Systems and Networks, Shanghai Jiao Tong University, Shanghai, China.

Feiran Su was born in Henan, China, in 1988. He received the B.E. degree from Shanghai Jiao Tong University, Shanghai China, in 2010, where he is currently working toward the Ph. D. degree in the State Key Laboratory of Advanced Optical Communication Systems and Networks, Department of Electronic Engineering. His research interests include microwave photonics and high-speed analog-to-digital conversion.

Xinwan Li (SM'08) received the M.S. degree from Shanghai University, Shanghai, China, in 1993, and the Ph.D. degree from Shanghai Jiao Tong University, Shanghai, in 2005. Since 1993, he has been with Shanghai Jiao Tong University, where he is currently a Professor. From 1997 to 1998, he was with Essex University, Colchester, U.K., as a Research Assistant. In 2001, he joined OPCOM, Inc., as an Engineer and as a Visiting Professor of Chonbuk National University in 2007. His main research interests include optical switching technologies and advanced optical fiber components. He is a Senior Member of the IEEE Photonics Society and the Chair of the IEEE Communications Society Shanghai Chapter.

Jianping Chen received the B.S. degree from Zhejiang University, Hangzhou, China, in 1983, and the M.S. and Ph.D. degrees from Shanghai Jiao Tong University, Shanghai, China, in 1986 and 1992, respectively, where he is currently a Professor with the State Key Laboratory of Advanced Optical Communication Systems and Networks, Department of Electronic Engineering. His main research interests include photonic devices and signal processing, optical networking, and sensing optics. He is also a Principal Scientist of the 973 project in China.